NANO · MICRO small
www.small-journal.com

Wide Dynamic Range Thermometer Based on Luminescent Optical Cavities in Ga_2O_3:Cr Nanowires

Manuel Alonso-Orts, Daniel Carrasco, José M. San Juan, María Luisa Nó, Alicia de Andrés, Emilio Nogales,* and Bianchi Méndez*

Remote temperature sensing at the micro- and nanoscale is key in fields such as photonics, electronics, energy, or biomedicine, with optical properties being one of the most used transducing mechanisms for such sensors. Ga_2O_3 presents very high chemical and thermal stability, as well as high radiation resistance, becoming of great interest to be used under extreme conditions, for example, electrical and/or optical high-power devices and harsh environments. In this work, a luminescent and interferometric thermometer is proposed based on Fabry–Perot (FP) optical microcavities built on Cr-doped Ga_2O_3 nanowires. It combines the optical features of the Cr^{3+}-related luminescence, greatly sensitive to temperature, and spatial confinement of light, which results in strong FP resonances within the Cr^{3+} broad band. While the chromium-related R lines energy shifts are adequate for low-temperature sensing, FP resonances extend the sensing range to high temperatures with excellent sensitivity. This thermometry system achieves micron-range spatial resolution, temperature precision of around 1 K, and a wide operational range, demonstrating to work at least in the 150–550 K temperature range. Besides, the temperature-dependent anisotropic refractive index and thermo-optic coefficient of this oxide have been further characterized by comparison to experimental, analytical, and finite-difference time-domain simulation results.

1. Introduction

Thermal management at the micro- and nanoscale is crucial in multidisciplinary fields of applications that require the control of heat flux and accurate temperature assessment, from opto-electronics up to biomedicine.[1–4] In this regard, the measurement of local temperature through optical transducing mechanisms is a quickly growing research area that allows for minimally intrusive temperature sensing, unlike other mechanisms such as electric ones. The criteria for the goodness of temperature sensors are sensitivity, dynamic range, precision, accuracy, or stability, among others, with a wide operating temperature range being one of the most challenging.[5] Taking this into account, several sensor platforms for optical thermometers have been recently attempted attending to specific underlying mechanisms, such as luminescence ratiometric or interferometry properties.[6–10]

Luminescent thermometers offer a variety of spectral features, as intensity of emission bands, bandwidth, emission ratio between different lines, spectral shift, or lifetime, which are affected by temperature-dependent mechanisms and hence can be used as quantitative observable parameters to be translated into a temperature value.[3] In this sense, up-conversion nanoparticles and quantum dots are taking the lead in the luminescent thermometry scenario offering reliable performances.[11] The high efficiencies and well-known emission lines from optically active ions, as rare-earth or transition metal ions, are some of the appealing features that make them very suitable for temperature studies.[5,12,13] Besides, several reported luminescence sensors cover wide temperature ranges.[2,14,15]

On the other hand, single nanowires (NW) and fibers have also been proposed for thermometers at the micro- and nanoscale via optical or electrical transducing mechanisms, although in the latter case electrical contacts are needed.[16–18] The elongated morphology of wires and fibers allows optical waveguiding and, hence, interference effects could be exploited for temperature sensing.[10] So, compact fiber gratings[19] or Fabry–Perot (FP) cavities[20,21] have also been proposed as optical interferometric thermometers. The reported FP cavities are mostly based on silica fibers and allow dynamic temperature ranges from room temperature (RT) upward by playing with the cavity length of the interferometer.[21]

In all cases, the morphology and knowledge of the material properties are of paramount importance in order to design high-performance thermometers at the micro- and nanoscale

M. Alonso-Orts, D. Carrasco, E. Nogales, B. Méndez
Departamento Física de Materiales
Fac. CC Físicas
Universidad Complutense de Madrid
Madrid 28040, Spain
E-mail: manalo01@ucm.es; enogales@ucm.es

J. M. S. Juan, M. L. Nó
Departamento de Física
Facultad de Ciencias y Tecnología
Universidad del País Vasco
Apdo. 644, Bilbao 48080, Spain

A. de Andrés
Instituto de Ciencia de Materiales de Madrid
Consejo Superior de Investigaciones Científicas
Cantoblanco, Madrid 28049, Spain

The ORCID identification number(s) for the author(s) of this article can be found under https://doi.org/10.1002/smll.202105355.

DOI: 10.1002/smll.202105355

capable of operating in a wide range of temperatures, from cryogenic to well above RT. In this sense, sensor platforms that allow for multiple optical transducing mechanisms are of the highest interest.

The incorporation of Cr^{3+} ions in a suitable crystal field matrix provides information about local temperature because of the electron–phonon coupling effects in the wavelength positions, intensity ratio, and decay time constants of their characteristic R-lines.[22,23] A recent report shows the potential of R-lines emissions in Cr^{3+}-doped $Bi_2Al_4O_9$ for ratiometric thermal sensors, with an improved performance with respect to rare-earth doped thermometers.[13] To this purpose, Ga_2O_3:Cr can be a good candidate for R lines-based ratiometric temperature sensors. Indeed, its behavior is expected to be better than that of Al_2O_3 or other oxides due to a lower site symmetry of the Cr^{3+} ion in Ga_2O_3, which results in a temperature resolution of around ± 1 K at 80–300 K.[23] This resolution is better than most of the temperature sensors in this low temperature range with applications in biological experiments (e.g., frozen cell experiments). Particularly, Ga_2O_3:Cr nanostructrures have been used for biological imaging application by virtue of their long lasting luminescence and low toxicity,[24,25] but have not been used as thermometers so far. Herein, we study Cr-doped gallium oxide NW as a single platform to develop robust and reliable optical thermometers with a dual transducting mechanism, that is, luminescence and optical interferometry.

β-Ga_2O_3 is a thermally and chemically highly stable material that has recently been shown to be very suitable for both high power electronics,[26] solar-blind ultraviolet (UV) photodetectors,[27] and high power optics in the nanoscale,[28] also in harsh environments.[29] In addition, it is an ultra-wide bandgap semiconductor (4.8 eV), which results in a wide transparency range which allows for a fine luminescence tunability over the near UV-visible-near infrared range (NIR) when doped with optically active ions, such as transition metals or rare earth ions.[30–33] In particular, Ga_2O_3:Cr is a very efficient red-NIR emitter due to the superposition of a broad phonon-assisted band and the aforementioned R-lines, which lie at around 1.78 and 1.80 eV. Both luminescence features are related to the Cr^{3+} intraionic transitions in Ga_2O_3: The broad band originates from the $^4T_2 - {}^4A_2$, while the sharp R-lines from the $^2E - {}^4A_2$ ones. The R-lines' wavelength positions, their intensity ratio, and their decay time constants are sensitive to the local temperature mediated by electron–phonon coupling mechanisms.[22,23]

The R-lines are clearly observed in the photoluminescence (PL) spectra of β-Ga_2O_3 up to about RT. On the other hand, the broad phonon-assisted PL band due to $^4T_2 - {}^4A_2$ transition is observed at temperatures above ≈ 100 K. For temperatures around 300 K onward, R-lines are hardly observed, as PL spectra are completely dominated by the broad band.[34,35] Fabrication of properly designed optical microcavities in the NW results in sharp FP resonances over this broad band. Their positions change with temperature mainly due to the variation of the refractive index and of the cavity length due to thermal expansion. Therefore, FP peak positions in this system are proposed as a very useful observable quantity for temperatures ranging from about 150 K to well above 300 K, potentially up to many hundreds Kelvin. This high temperature range is needed for key applications in industries such as high power electronics and high power photonics, where Ga_2O_3 is a very competitive material. Hence, it is considered of great interest to fabricate a temperature sensor with good temperature and spatial resolution, capable of operating in a wide temperature range, both at cryogenic and at high temperatures, based on Ga_2O_3. Optical interferometry thermometers based on shifts of well-defined resonant peaks, which can be designed to be more accurate than ratiometric sensors, could bridge the gap between the lower and higher temperature ranges, and would be desirable for such applications.[10] Previous works have demonstrated the feasibility of building optical microcavities based on β-Ga_2O_3:Cr micro- and NW in which tailored Distributed Bragg Reflectors (DBR) have been used as optical mirrors of the cavity.[36,37] These cavities show sharp FP resonance peaks of high finesse due to the high reflectivity at the DBRs. These features support the strong potential of taking advantage of the optical properties of Cr^{3+} ions in β-Ga_2O_3 for multimodal temperature sensing.

In this work, we propose to exploit the optical properties of β-Ga_2O_3:Cr DBR microcavities to be used as local thermometers over a wide range of temperatures from cryogenic up to high temperatures (150–550 K). The transducing mechanisms involved are the intrinsic luminescence of the Cr^{3+} ions as well as the interference effects of light confined in the FP cavity. Both R-lines and FP resonances are affected by local temperature and can be used as multimodal temperature sensor. In the interferometric mode, the spectral shift of the resonant peaks can be nearly linear fitted with the temperature, which allows for a simple calibration of this method. Furthermore, it allows to extend the measurement range well beyond RT with micron-scale spatial resolution.

2. Results and Discussion

Figure 1a,b shows SE images of a DBR-based cavity fabricated in a Ga_2O_3:Cr NW with 730 nm width and 620 nm depth dimensions, with an irregular hexagonal cross section.[37] The two focused ion beam (FIB)-fabricated DBRs consist of ten holes each one, periodically drilled in the NW with a periodicity of Λ = 470 nm, separated by an unpatterned region with length L = 13.0 μm that becomes the optical cavity. The parameters that define the DBRs were chosen to optimize the interference for Cr^{3+} emission using finite-difference time-domain (FDTD) simulations. Previous work on the structural characterization of Ga_2O_3 NW obtained by this thermal method concluded that the crystalline phase is the monoclinic β-Ga_2O_3.[36] These wires may exhibit certain anisotropy in their optical and thermal properties due to the monoclinic crystalline lattice. Taking this into account, polarized Raman measurements have been carried out to assess the crystallographic orientation of the axis wire and the surface planes, which will be necessary to further discuss light confinement effects in the microcavity. A fixed polarizer was used in order to set parallel the incident laser and scattered light polarizations. A plan-view sketch of the used configuration is shown in the inset of Figure 1c, where the arrow indicates the polarizer axis and the blue rod represents the wire. By rotating the wire, angle-resolved Raman spectra can be achieved by recording data at different angles between the wire and the polarizer. Figure 1c shows polarized Raman spectra for two extreme angles, almost

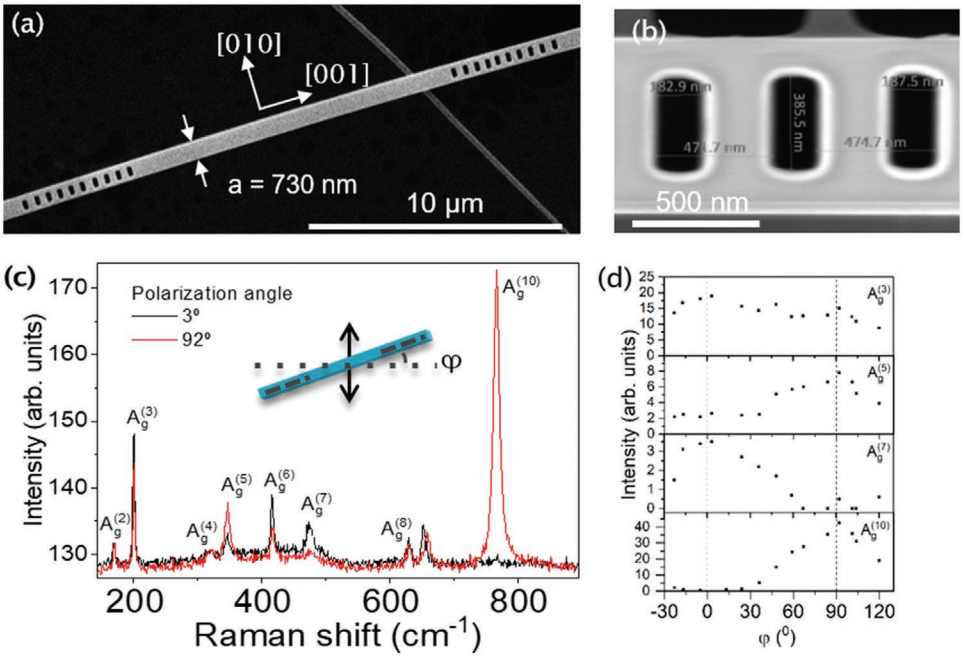

Figure 1. a) SE image of the Ga_2O_3 DBR microcavity. b) Detail of three of the periods which form the DBRs. c) Polarized Raman spectra from the wire for two different polarization angles, ϕ. Inset: Plan-view sketch of the used configuration. The arrow shows the direction polarization of both excitation and detection signals. $\phi = 0$ is defined perpendicular to the wire axis. d) Intensity versus polarization angle for $A_g^{(3)}$, $A_g^{(5)}$, $A_g^{(7)}$, and $A_g^{(10)}$ Raman peaks.

parallel (black line) or perpendicular (red line) to the polarizer. The main peaks are identified as the usual Raman modes observed in β-Ga_2O_3.[38,39] It can be clearly seen that the intensity of some peaks changes dramatically as the angle varies. Figure 1d shows the intensity dependence on the rotation angle for some peaks. In particular, the angle dependence in $A_g^{(7)}$ and $A_g^{(10)}$ modes, which present maxima at 0° and 90°, while a null intensity at 90° and 0°, respectively, can be used to assess the crystal directions of the wire. The angular dependence for all the modes observed in Figure 1c can be found in the Figure S1, Supporting Information. The results are in agreement with the angular dependence observed for this polarization configuration in β-Ga_2O_3 crystals with (100) surface and the $\phi = 0°$ angle defined parallel to the [010] direction.[39] Therefore, we conclude that the wire axis direction is [001], which is perpendicular to [010] in monoclinic Ga_2O_3 crystal structure. These orientations are also indicated in Figure 1a.

The energy levels of Cr^{3+} ions in Ga_2O_3 are represented schematically in **Figure 2**a. The complete configurational coordinate diagram was reported in ref. [34]. The RT luminescence of as-grown Cr doped Ga_2O_3 wires is composed of sharp R-lines and a broad phonon-assisted band, as a result of the transitions from the excited ^2E and $^4T_2$ levels to the ground $^4A_2$ one, respectively. The ^2E is actually split into the $\overline{E}$ and the $2\overline{A}$ sublevels; hence, two sharp R-lines can be resolved. The energy difference, ΔE, between the ^2E and the $^4T_2$ levels, has been found to be around 60 meV in NWs,[34] and similar values are reported in bulk Ga_2O_3.[35] This energy difference determines the temperature-dependent intensity ratio between the R-lines and the broad band. On the other hand, the broad emission band arising from transitions between $^4T_2$ and $^4A_2$ levels provides a wide range of wavelengths susceptible to be confined efficiently, if the geometry of the cavity matches the FP resonance condition. Actually, the confinement of the emitted light between the two DBRs brings about FP resonances that strongly enhance specific wavelengths of the broad band.

The electronic levels configurations in Ga_2O_3:Cr wires in which two DBRs delimit an optical cavity give rise to the RT micro-PL spectrum shown in Figure 2b. The peaks at 689.8 and 696.6 nm (1.80 and 1.78 eV, respectively) correspond to the R-lines (R1 and R2), while the peaks at 714.2 nm (labeled #1), 723.0 nm (labeled #2), 732.1 nm (labeled #3), and 741.3 nm (labeled #4) are the four most intense FP resonances of the optical cavity. The reflectivities at the DBRs ends reach up to R = 73 % and lead to finesse values, up to $F = 10$, which points out that the optical resonances are very well defined in this NW-based optical cavity. This is relevant for thermometric measurements since the spectral shifts of these peak positions are the observable quantity, and hence, the sharper the resonances, the better the thermometer resolution.

Therefore, the features observed in the PL spectra of Ga_2O_3:Cr optical cavities, highlighted in red dotted boxes in Figure 2b, make them very suitable to be used as temperature sensor, grounded in two reasons. First, the large Stokes shift, for example, the difference in energy between excitation and emission photon energies, and the observation of a broad band at temperatures above ≈100 K, whose width increases with temperature, both consequences of the strong electron-phonon coupling in Ga_2O_3:Cr. Due to these coupling effects, the R-lines positions and their relative intensities vary with temperature, as it will be shown next. Second, the optical resonances produced on the broad phonon-assisted band in the Ga_2O_3:Cr microcavities may be strongly affected by temperature by the variation of the refractive index and the Ga_2O_3 lattice thermal expansion with

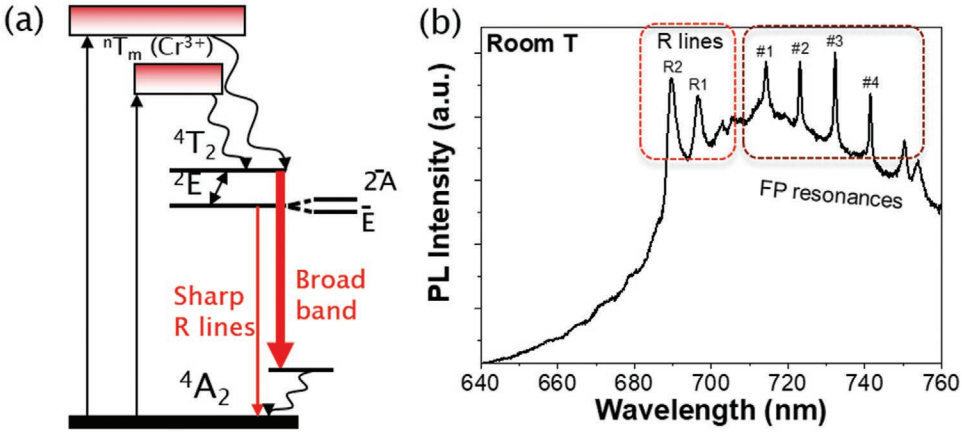

Figure 2. a) Cr^{3+} energy levels qualitative diagram in Ga_2O_3. b) RT overall μ-PL spectrum recorded from the cavity showing both R-lines and resonant peaks over the broad phonon-assisted band.

temperature, as we will discuss later. Therefore, the exploitation of these features drives the design of a local optical thermometer.

It is worth mentioning that each of these two main features are relevant in different temperature ranges. R-lines are pretty well resolved and dominant at low temperatures, while the broad phonon-assisted band becomes dominant from RT onward. Since the optical resonances occur over this band, the measurement of the spectral shifts of the resonant peaks would be effective at high temperatures. In summary, this platform is able to provide local temperature information in a wide range of temperatures due to both luminescence and interferometric effects, just from a single nanostructure.

2.1. R-Lines Emission

There are several outputs in the R-lines PL capable to be translated into temperature values, such as emission intensity, spectral shift, full width at half maximum (FWHM), or decay times. As a function of the host and the observable parameter of choice, the temperature resolution differs.[2,40] Up to now, intensity ratio and decay times have been considered among the best indicators to be used in optical temperature sensors, and the best results are reported for cryogenic temperatures (40–140 K),[23] mainly because the R-lines become partially hidden under the phonon-assisted band as temperature increases. In the case of NWs, the Cr-related emission is relevantly enhanced, even for unintentionally doped material,[41] which would allow us to monitor R-lines up to RT, at least.

Figure 3 shows a series of detailed μ-PL spectra of the Ga_2O_3:Cr cavity over the R-lines range for several temperatures between 150 and 400 K, stabilized by the cooling system. In this range, the most convenient parameter to follow is the peaks positions. **Table 1** shows the R-lines' wavelength positions measured from the PL spectra in the temperature range from 150– 400 K. **Table 2** shows the temperature coefficients, $\Delta\lambda_{R2}/\Delta T$, when using the spectral shift of R2 line. The observed spectral shift as the temperature increases is attributed to the electron–phonon interaction, whose strength depends on the phonon population,[23] and hence, ultimately on temperature. In particular, the spectral shift of R2 line can be used as temperature sensor with an acceptable temperature coefficient of around 8 pm K^{-1}. Taking into account the precision of the spectroscopy system is better than 0.01 nm, the temperature resolution achieved by measuring the position of the R2 line in our Cr-doped wire is about 1.5 K, within the temperature range 150–400 K.

These results are quite competitive in comparison with very recent work reported on potential Ga_2O_3:Cr thermometers based on bulk crystals[22] and optical fibers.[23] In these works, R-lines intensity, spectral shift of maxima, half-width, and lifetime have been measured as a function of temperature. Luchechko et al. proposed this Ga_2O_3:Cr as potential thermometer in

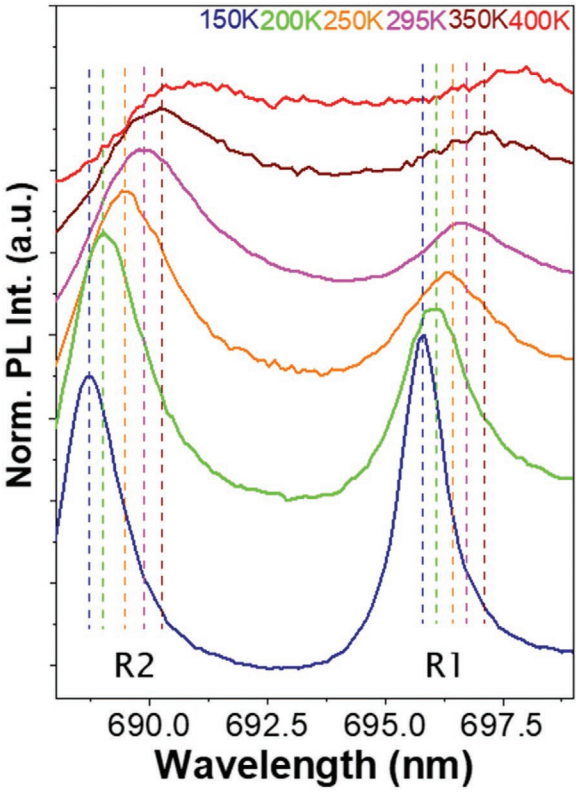

Figure 3. Micro-PL spectra of the cavity showing the R lines with respect to the temperature defined by the cooling system in the interval 150–400 K.

Table 1. R lines positions with respect to the temperature defined by the cooling system.

Temperature [K]	λ_{R2} [nm]	λ_{R1} [nm]
150	688.70	695.8
200	689.02	696.0
250	689.46	696.3
295	689.87	696.7
350	690.25	697.1

the range close to liquid nitrogen temperature (100–160 K), based on the temperature dependence of the R-lines luminescence decay time.[22] On the other hand, Mykhaylyk et al. extended the temperature range by monitoring the luminescence intensity ratio between 40–140 K and decay time constant in the 80–300 K interval, in such a way that the overall temperature range could be widened up to RT. The best temperature resolution achieved (better than ±1 K) was in the low temperature range, whereas from 150–300 K, the temperature resolution is reported to be above 2 K.[23] It should be noted that the temperature coefficient and resolution do not generally depend linearly on temperature. Hence, it would be important to know this function to assess the quality of the thermometer.

2.2. Fabry–Perot Resonances Spectral Shift

As it has been mentioned above, the Ga_2O_3:Cr nanowire can be converted into a tunable resonant cavity by a suitable patterning of DBRs. The phonon-assisted broad band related to Cr^{3+} $^4T_2 - {}^4A_2$ transitions of the Ga_2O_3:Cr microwire provides photons in the 650–800 nm wavelength range susceptible to promote resonances within the optical cavity, as it has been shown in Figure 2b. Here, we demonstrate that the spectral shift of these resonant peaks are an excellent choice to be used as an observable for temperature sensing. Furthermore, the calibration curve is provided. Moreover, during the study, intrinsic temperature-dependent optical coefficients of Ga_2O_3 have been determined from the comparison among experimental, simulations, and analytical results.

Figure 4a shows partial PL spectra detailing the shift of resonant peaks #2 and #3 (see Figure 2b) in the 150–400 K temperature range. The spectral shift is seen to be quite larger than that observed for the R lines. Hence, monitoring the resonances' spectral shift is expected to provide a good temperature resolution in temperature sensors. Importantly, the line-shape of the FP peaks does not essentially change in the studied temperature range, as will be discussed below. To get a more complete picture, Figure 4b shows a contour map of the PL spectra of the main four resonances of the DBR cavity, displayed in Figure 2b, as a function of the temperature. The results show a monotonic wavelength redshift as temperature increases for all resonant peaks. The apparent step at 300 K is due to the fact that two set of spectra were used, one below 300 K obtained under vacuum conditions in the cryostat, and the other above 300 K in air.

Table 2. Temperature coefficient of the thermometer based on the position of the R2 line at different temperatures.

Temperature [K]	$\Delta\lambda_{R2}/\Delta T$ [pm K^{-1}]
150–200	6.4
200–250	8.8
250–295	8.2
295–350	6.9

From this contour map, the spectral shift dependence with temperature can be deduced for each resonant peak. Figure 4c shows the spectral shifts, from the peak positions at 300 K, for the three main FP peaks, #2, #3, and #4, represented by squares. The experimental data present a quasi-linear behaviour and can be pretty well fitted to a quadratic expression, as shown with solid lines. The fitting parameters of the curves are indicated for each peak, A and B being the relevant ones for thermometry purposes. The values of these parameters are quite similar for the three peaks, although a slight increase is obtained for the linear parameter, B, when increasing the peak number. From these curves, the temperature coefficient, $d\lambda/dT$, of our device can be calculated for different temperatures. **Table 3** shows the calculated values for different temperatures from the spectral shifts of peaks #2, #3, and #4. These figures are similar to those reported in silica tapered or micrograting fibers by analyzing the temperature dependent reflectance oscillations, where experimental values of 17 or 22 pm K^{-1} were obtained.[19,20] Due to slight deviation from the linear dependence, this coefficient varies from 9.5 pm K^{-1} at 150 K up to 15 pm K^{-1} at 400 K. By extrapolation, it is expected to reach a value of 20 pm K^{-1} at 600 K. Taking into account the accuracy of the experimental system to determine the wavelength positions of the much narrower PL peaks compared to the reflectance oscillations, the temperature resolution achieved along the whole temperature range is around 1 K or better as discussed below.

The spectral shift of the resonant cavity modes with increasing temperature in FP cavities is due to changes in the intrinsic properties of the material.[42] In particular, the wavelength shift when light is perpendicularly incident on the mirror surfaces can be expressed as:

$$\frac{d\lambda_m}{dT} = \lambda_m \left\{ \frac{1}{n}\frac{dn}{dT} + \frac{1}{L}\frac{dL}{dT} \right\} = \lambda_m (\delta + \alpha) \quad (1)$$

where n is the refractive index, L the cavity length, δ the thermo-optic coefficient, and α the thermal expansion coefficient of the material.[42] For a more general case, such as our microcavities, where light is waveguided along a wire with lateral dimensions of the order of the wavelength, the wavevector **k** is not perpendicular to the mirror surfaces and the shift calculation is not so straightforward.

As a first approximation, the temperature coefficients, Table 3, derived from experiments can be compared with those obtained from the theoretical model summarized by Equation (1). The thermo-optic, $\delta \approx 3.7 \times 10^{-5}$ K^{-1}, and thermal expansion coefficients $\alpha_{c^*} \approx 5.35 \times 10^{-6}$ K^{-1}, were reported for gallium oxide single crystals in the 303 – 443 K temperature and the 700 – 750 nm wavelength ranges.[43,44] With these parameters, the expected resonant wavelength blueshift for perpendicularly

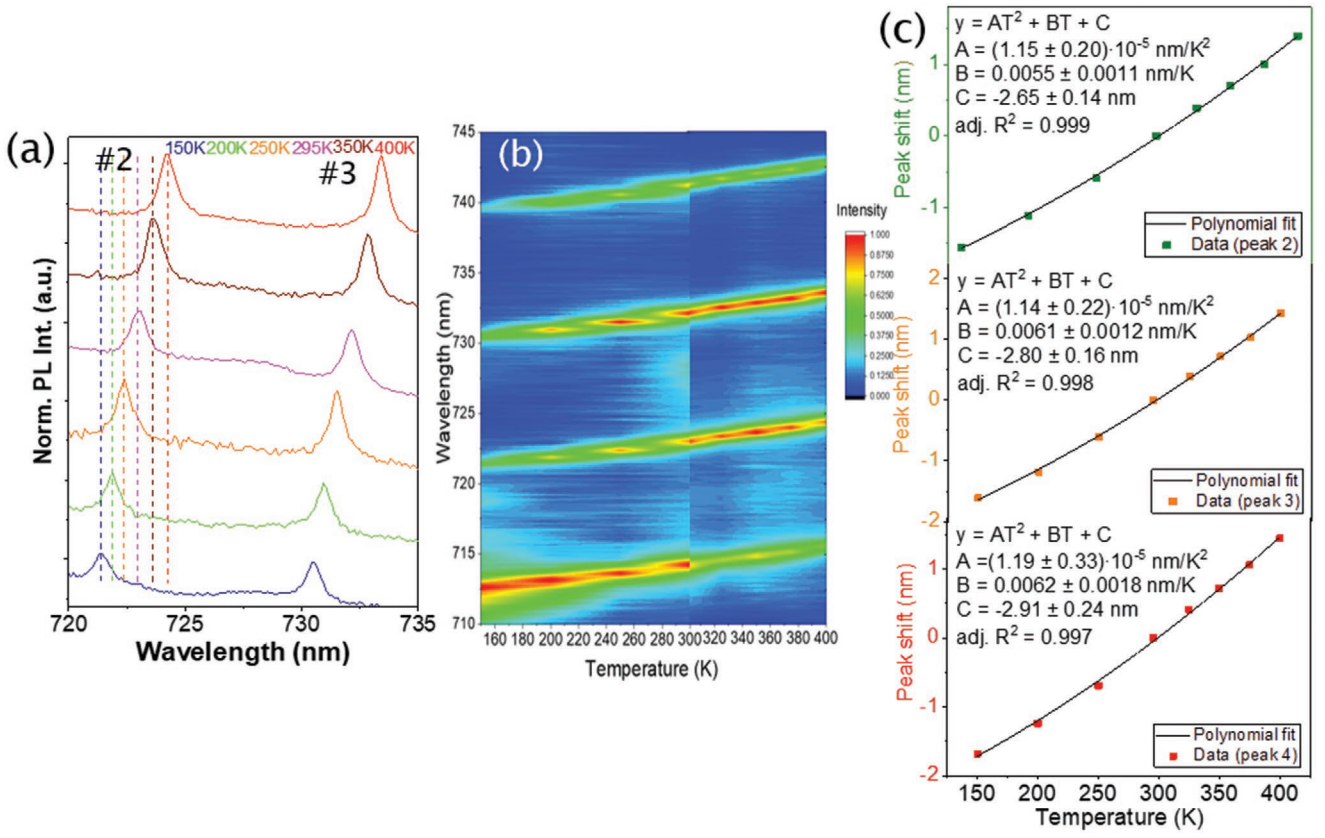

Figure 4. a) Resonant peaks #2 and #3, labeled in Figure 2b, recorded at different temperatures. b) Contour plot of PL spectra in the 710–745 nm range as a function of temperature, in which a quasi-linear redshift of four resonant peaks is clearly observed. c) Resonant peak shifts with respect to temperature for peaks #2, #3, and #4. Zero shift has been set at 295 K. The squares are the experimental results while the solid lines show the quadratic fitting of each of the peak shifts, whose equations and fitting parameters are also shown.

incident waves in this wavelength range at T ≈ 300 K would be around 30 pm K^{-1}, as obtained from Equation (1). This value is more than twice that obtained from our experimental data. However, as it has already been mentioned, this shift should be influenced by the fact that light is guided and **k** is not parallel to the wire axis. Therefore, a deeper study is needed in order to take into account the anisotropy of the refractive index of β-Ga_2O_3, the wire morphology, and the crystal directions, defined in Figure 1 from polarized Raman analysis. To this purpose, we have carried out both simulations and analytical calculations of the resonant modes in the optical cavity at different temperatures and compared them with the experimental results.

The simulations were performed with the OptiFDTD commercial software by Optiwave, where the anisotropy of β-Ga_2O_3 crystal and the crystal directions obtained from polarized Raman measurements (Figure 1d and Figure S2, Supporting Information) can be considered. It should be mentioned that a thermal expansion of 5 nm, as obtained from α_{c^*}, L, and ΔT, in the cavity has been estimated at 398 K with respect to RT, in the simulations. Thermal expansion of the transverse dimensions has been neglected. The temperature dependence in the simulations was incorporated by the variation of the refractive index dispersion relation, $n(T)$, in the Sellmeier equations (see Supporting information). The dispersion relations used were those reported by Mu et al. at RT,[43] and by Bhaumik et al. at 303 and at 398 K,[45] which are represented by red lines (398 K) and black lines (303 K) in Figure 5a. The details of the simulations can be found in Section SII, Supporting Information. The comparison between experimental results (squared dots) and simulations (solid lines) at RT and 398 K for peak #3 are shown in **Figure 5**b. At RT (in black), the experimental and simulated data are well matched, but with a slight shift due to the 8 K difference between measured spectrum, 295 K, and reported parameters, 303 K. However, the actual resonance shift (red squares) when increasing the temperature up to 398 K is not accurately predicted from the dispersion relations shown above (red solid line). This could be due to an incorrect $n(\lambda)$ function at 398 K. Therefore, we have run additional FDTD simulations fitting the parameters of the dispersion relation in order to match our experimental results at 398 K. The output of this simulation is represented as the green line in Figure 5b, where a nice agreement with the experimental results is clearly seen. The final dispersion curves that match experimental data and simulation results at 398 K are shown in the green curves in Figure 5a. The fitting parameters are included in Table S1, Supporting Information.

On the other hand, the resonant peaks in the cavity can also be obtained from the analytical expressions in the framework of Marcatili model,[36] as explained in Section SIII, Supporting

Table 3. Temperature coefficients calculated from the spectral shifts of peaks #2, #3, #4, obtained from the fits shown in Figure 4 at different temperatures.

	#2	#3	#4
T [K]	$d\lambda/dT$ [pm K^{-1}]	$d\lambda/dT$ [pm K^{-1}]	$d\lambda/dT$ [pm K^{-1}]
150	8.9	9.5	9.8
295	12.3	12.8	13.2
400	14.7	15.2	15.7
600	19.3	19.8	20.5

Information. Marcatili model is an approximation that uses an isotropic refractive index. However, monoclinic gallium oxide presents an anisotropic refractive index, as detailed above; thus, an average refractive index was used, averaging n_x, n_y, and n_z. The analytical calculations have been made for both RT and 398 K, for which the average n values are obtained from the relationships of Figure 5a. The sets of equations for the dispersive relations for k_x and k_y, plus the FP resonance condition for the k_z component, are solved by fixing an appropriate effective cavity length. The parameters used in this analytical approach as well as the resonance peak position at RT and 398 K for the peak #3 are shown in Table S2, Supporting Information. Vertical arrows in Figure 5b indicate the position of the peaks at RT (black arrow) and at 398 K (red arrow and green arrows), obtained from this analytical method. It can be seen that this approximation results in wavelength shifts close to those obtained by simulations, although slightly over-shifted.

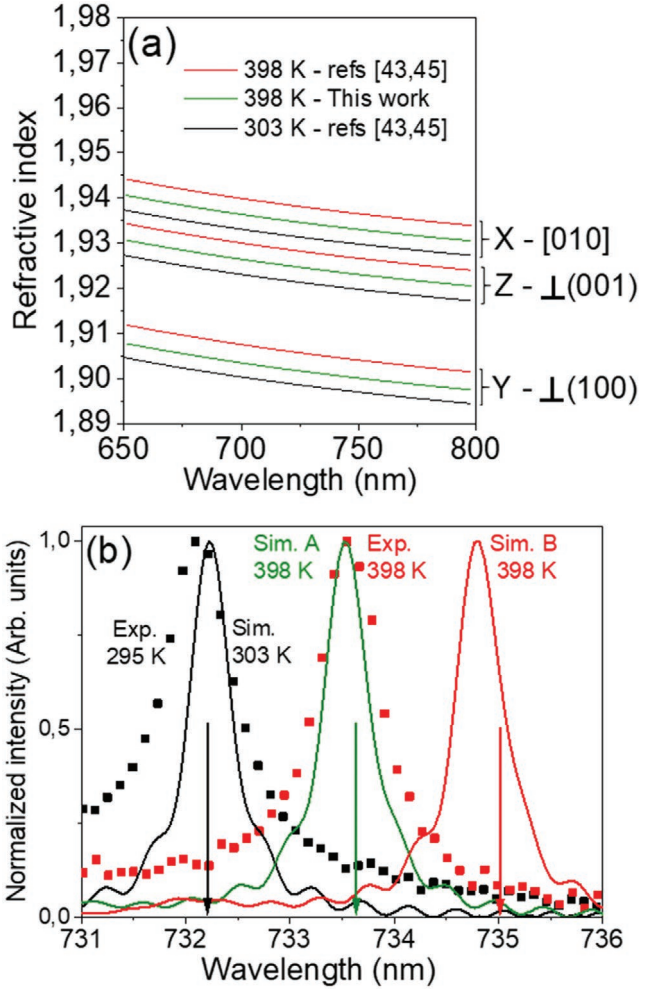

Figure 5. a) Dispersion relations used for the simulations at 295 and 398 K, based on refs. [43,45] in black and red lines. Green solid lines are the ones proposed in this work to fit the experimental shifts. b) FDTD simulations (lines) versus experimental results (square dots) of the peak #3 shift at RT and 398 K. Simulated shift by using the dispersion relations based on refs. [43,45] is displayed in red color (Sim B), whereas simulations with the proposed dispersion relation at 398 K in this work (Sim A) is displayed in green color. Finally, vertical arrows indicate the peak position as obtained from the analytical approximation.

Therefore, from this work, a temperature-dependent anisotropic refractive index, $n(\lambda)$, of β-Ga_2O_3 is proposed in the 650–800 nm wavelength range (green lines in Figure 5a). These results also provide the value of the thermo-optic coefficient at 732 nm, $(dn/dT)/n = 1.77 \times 10^{-5}$ K^{-1}.

2.3. Local Heating Assessment

Finally, in order to assess the robustness of the DBR optical cavity as a temperature sensor, the issue of the local heating due to the laser irradiation needs to be addressed. The local heating assessment is quite relevant to evaluate the limits of this thermometry method and to avoid artifacts in the temperature measurement. In addition, it would be very valuable to verify the stability of these optical cavities at higher temperatures than those accessible with our heater (400 K). The latter would be expected since monoclinic β-Ga_2O_3 exhibits a high stability at temperatures higher than 1000 °C.[46]

For this purpose, PL spectra from the cavity have been recorded under excitation with 325 nm (UV) and 488 nm (blue) lasers, with maximum excitation power of 0.4 and 11 mW, respectively (**Figure 6**). We have inserted neutral optical density filters in the optical path of the incident laser and/or reduced their output power, thereby reducing the excitation power density.

Figure 6a shows the normalized PL results, using the UV laser at RT, for 100% and 1% pump powers, showing an evident red-shift of the R-lines and the resonant modes in the full power (100%, violet line) spectrum with respect to the 1% (orange one). Therefore, a clear local temperature increase can be inferred when the laser is at full power. By using optical filters, an evolution of the intermediate heating can be analyzed, as observed in the top panel of Figure 6c, which shows a zoom in of resonant peak #3 for optical filters decreasing the incident power to 1%, 10%, 25%, and 50%. On the other hand, Figure 6b shows the PL spectra excited with the blue laser, 488 nm excitation line. The nominal RT spectrum with an excitation power of 0.17 mW is shown in brown line, whereas the blue line shows the spectrum obtained at nominal 390 K by exciting with 11 mW power. The obtained local T change provokes a complete quenching of the R lines as well as a large shift of the FP peaks ($\Delta\lambda_3$ = 3.77 nm). Figure 6c shows a comparison of the peak position shifts at nominal RT exciting with each laser (top and middle panel), as well as at nominal 390 K (lower panel), for the different excitation conditions.

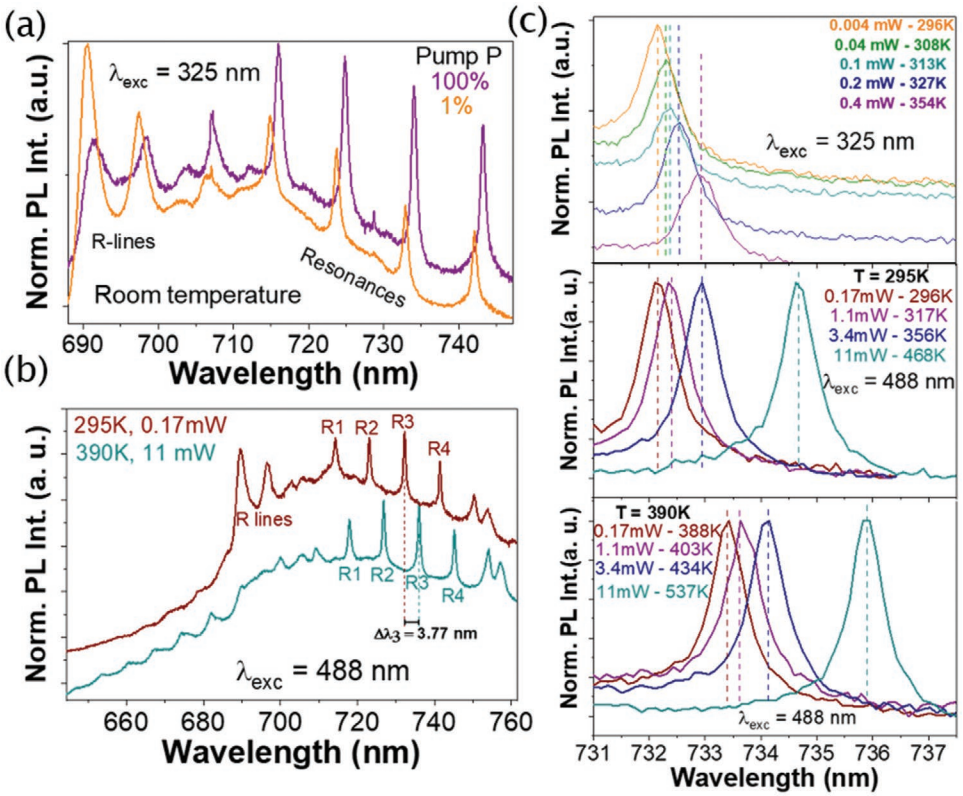

Figure 6. PL spectra for increasing power laser irradiation. a) RT PL using the UV laser, 325 nm line, with 100% pump power (purple) and 1% pump power (orange). The spectra are vertically shifted for clarity. b) Blue laser, 488 nm line, at nominal 295 K and 0.17 mW (brown) and nominal 390 K and 11 mW (blue). c) Comparison of the peak position exciting with each laser line at nominal RT (upper and middle spectra), as well as at nominal 390 K (lower spectra), for different excitation powers. In all the spectra, the peak intensities are normalized, and the peaks in the upper spectrum are vertically shifted for clarity. The calculated temperature from the peak position for each power is indicated.

According to calibration curves displayed in Figures 4b,c, the position of the peak #3 at 295 K is 732.1 nm. This value matches pretty well with the obtained position of this resonant peak when exciting with the UV laser at 1% pump power (Figure 6c top panel, orange line). Moreover, the relative intensity of the R-lines for 1% UV pump power is very similar to the value obtained with the 488 nm laser and the results reported in ref. [22]. Therefore, we can conclude that the UV laser at 1% pump power does not heat the cavity and temperature is kept at 295 K, that is, the temperature is not locally affected by the laser beam for this incident power. However, when the laser power is increased, a monotonic red-shift is observed, as shown in Figure 6c for 10%, 25%, 50%, and 100% incident pump powers, which fits with a local heating of the cavity. This behavior is reversible in the sense that when changing the excitation density of the laser, the expected shifts in the resonant peaks are observed.

By using the quadratic fits shown in Figure 4c, and supposing that the whole cavity is heated up to the same temperature, a precise estimation of the local temperature can be obtained for each laser pump power, as deduced from the peak positions. **Table 4** summarizes the results of the local heating assessment of the cavity as a function of the laser pump power. The peak position shifts indicate that a maximum temperature increase of 58 K is reached due to heating with the UV laser in the current conditions, while a temperature increase of 172 or 149 K is obtained when heating with the blue laser, starting from RT and 390 K, respectively.

Finally, it is worth mentioning that, differently to other spectral peak shifts used in thermometry, the FWHM of our FP peaks does not essentially change in the whole studied

Table 4. Wavelength position of FP resonant peak #3 under different lasers and pump powers and its associated local temperature according to the quadratic fits in Figure 4c.

325 nm laser	Nominal 295 K	
pump P [mW]	λ_3 [nm]	Calculated T [K]
0.004	732.12	296
0.04	732.28	308
0.1	732.24	313
0.2	732.53	327
0.4	732.91	354

488 nm laser	Nominal 295		Nominal 390 K	
pump P [mW]	λ_3 [nm]	Calculated T [K]	λ_3 [nm]	Calculated T [K]
0.17	732.12	296	733.41	388
1.1	732.40	317	733.63	403
3.4	732.93	356	734.11	434
11	734.66	468	735.89	537

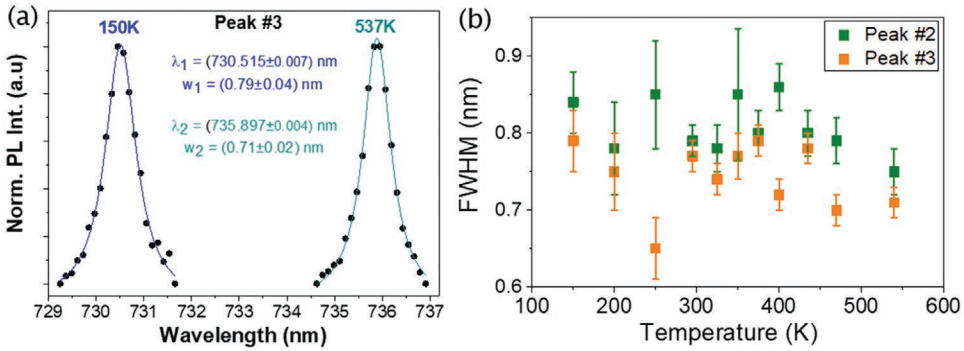

Figure 7. a) Lorentzian deconvolution of peak #3 at 150 K under 0.17 mW excitation power (dark blue line) and at nominal 398 K under 11 mW excitation power (light blue line). b) FWHM of resonant peaks #2 and #3 with respect to temperature. Error bars show the uncertainty of the Lorentzian fitting.

temperature range, from 150 K to the calculated nearly 550 K. **Figure 7**a shows the Lorentzian deconvolution of the resonant peak #3 at 150 K under low excitation power and at nominal 390 K under high excitation power (which results in 537 K local temperature, Table 4). It can be seen from the fitting results that their FWHMs are very similar. Figure 7b shows this parameter for peaks #2 and #3, with respect to the local temperature, showing a very similar peak FWHM in the whole local temperature range within the experimental error. This is a noticeable advantage, since the large widening and/or background increase of other optical signals with temperature is detrimental for the precision in the determination of the peaks' parameters (position, FWHM, and intensity). As this is not happening in the system presented in this work, the actual temperature resolution of the thermometers is virtually temperature independent. An estimation of the temperature resolution has been made by dividing the experimental error in the peaks position, as obtained by the fitting to Lorentzian, for example, 0.007 nm, as shown in Figure 7a, into the temperature coefficients $d\lambda/dT$, for example, 10 – 20 pm K^{-1} =0.01 – 0.02 nm K^{-1} for peak #4, as shown in Table 3.[23] This results in values of the temperature resolution slightly below 1 K for our system.

3. Conclusion

In conclusion, a robust and reliable remote optical thermometer with dual transducing mechanisms, luminescent and interferometric, based on highly stable β-Ga_2O_3:Cr optical microcavities is shown and analyzed. This oxide is quite relevant technologically for high power electronics and photonics. The optical proposed thermometer combines a micron range spatial resolution with a wide temperature range applicability. The red-NIR strong luminescence features provided by Cr^{3+} dopant in this oxide, that is, the sharp R lines and the broad phonon-assisted band, combined with FP resonances tuned to result in sharp peaks on the latter band, are the base for the observable quantities used for thermometry in this system. The R lines position is used for sensing low and intermediate temperatures, while the peak position of the FP resonances allows for sensing intermediate and high temperatures. The nearly linear calibration curve has been obtained for the FP-based thermometry, showing competitive temperature coefficients, around 15 pm K^{-1} at RT, and a resolution around 1 K or below in a temperature range between at least, 150 and 550 K. The comparison between the experimental results and detailed simulations, as well as analytical models, allowed to calculate the variation of the anisotropic refractive index of β-Ga_2O_3 with temperature, obtaining a thermo-optical coefficient at 732.1 nm of δ = 1.77 10^{-5} K^{-1}. The operation as thermometer of the designed microcavity has been demonstrated to be stable up to at least 550 K.

4. Experimental Section

Optical Cavity Fabrication: Ga_2O_3:Cr micro- and NW were obtained by a thermal evaporation method in a single-step treatment using metallic gallium and chromium oxide powders as precursors, as described elsewhere.[47] This procedure produces a high amount of β-Ga_2O_3 (i.e., monoclinic phase) micro and NW with a Cr doping concentration of around 0.5 at%. Then, the fabrication of the optical cavities was performed by milling with a FIB microscope a certain number of holes on an individual Ga_2O_3:Cr wire suspended on a transmission electron microscope grid.[36] The pattern was designed to create an optimized FP optical cavity of length L between two DBRs acting as mirrors.

Characterization Methods: The details of the morphology were assessed by secondary electron (SE) images obtained in a FEI Inspect scanning electron microscope. The DBR patterns were carried out with the aid of a FIB Helios 650 instrument working at 30 kV and 8 pA.

Two systems were used for micro-PL (μ-PL) measurements. For RT and above, a 325 nm He-Cd laser in the Horiba LabRAM HR800 optical confocal microscope was used. This equipment allows the separation of excitation and collection points up to several microns, thanks to a custom-made setup.[36] In addition, the crystallographic orientation of the axis and the surface planes of the Ga_2O_3 wires have been obtained from polarized Raman measurements in the Horiba LabRAM HR800 optical confocal microscope. Low- and high-temperature micro-PL measurements were obtained in a confocal system with the 488 nm line of an argon laser, an Olympus microscope with a 50x objective, a Super-Notch-Plus Filter, and a Peltier cooled CCD Synapse detector coupled to a Horiba monochromator. The sample was mounted in a continuous flow cryostat from Oxford Instruments or on a hot plate for heating measurements. All the μ-PL spectra were recorded with a polarizer placed perpendicular to the wire axis, which corresponds to the intrinsic polarization of the main confined optical modes within the cavity.[36] In this way, the relative intensity of the optical resonances with respect to the unconfined luminescence is maximized.

Simulations and Analytical Methods: The modal analysis of the optical microcavities was assessed by simulations performed with the OptiFDTD commercial software by Optiwave using the FDTD method. The simulation was performed with spatial mesh dimensions of 30 nm in X, 30 nm in Y, and 5 nm in Z directions. Time steps are defined to be 10^{-17} s and 400.000 steps were carried out for these simulations. A short pulse was allowed to propagate from a specific position within the cavity and the power spectrum, as a function of wavelength, was recorded at the middle of the cavity. A sketch is shown in the Supporting Information. In addition, analytical expressions based on Marcatili's method for rectangular waveguides were used in order to make a first approximation of the resonances (see Supporting Information).

Supporting Information

Supporting Information is available from the Wiley Online Library or from the author.

Acknowledgements

This work was supported by MICINN projects (RTI2018-097195-B-I00 and RTI2018-096918-B-C41). The authors acknowledge the financial support of the excellence research network MAT2016-81720-REDC, "RED IMAGINE" and project RED2018-102609-T by MINECO. The authors also acknowledge the use of the FIB facilities from the general services, SGIKER, of the University of the Basque Country. The authors also acknowledge the support from the Air Force Office of Scientific Research under Award No. FA8655-20-1-7013 (Program Manager: Ali Sayir). M.A-.O. acknowledges financial support from MICINN (FPU contract No. FPU15/01982).

Conflict of Interest

The authors declare no conflict of interest.

Data Availability Statement

The data that support the findings of this study are available from the corresponding author upon reasonable request.

Keywords

distributed bragg reflector optical cavity, Fabry–Perot resonances, gallium oxide, wide range thermometer

Received: September 2, 2021
Revised: October 14, 2021
Published online:

[1] *Thermometry at the Nanoscale*, (Eds: L. D. Carlos, F. Palacio), Nanoscience & Nanotechnology Series, The Royal Society of Chemistry, London **2016**.
[2] C. D. S. Brites, P. P. Lima, N. J. O. Silva, A. Millán, V. S. Amaral, F. Palacio, L. D. Carlos, *Nanoscale* **2012**, *4*, 4799.
[3] A. Bednarkiewicz, L. Marciniak, L. D. Carlos, D. Jaque, *Nanoscale* **2020**, *12*, 14405.
[4] F. Lahoz, I. R. Martín, D. Walo, R. Freire, J. Gil-Rostra, F. Yubero, A. R. Gonzalez-Elipe, *Appl. Phys. Lett.* **2017**, *111*, 111103.
[5] C. D. S. Brites, K. Fiaczyk, J. F. C. B. Ramalho, M. Sójka, L. D. Carlos, E. Zych, *Adv. Opt. Mater.* **2018**, *6*, 1701318.
[6] M. Back, E. Trave, J. Ueda, S. Tanabe, *Chem. Mater.* **2016**, *28*, 8347.
[7] M. Back, J. Ueda, M. G. Brik, T. Lesniewski, M. Grinberg, S. Tanabe, *ACS Appl. Mater. Interfaces* **2018**, *10*, 41512.
[8] M. Back, J. Ueda, H. Nambu, M. Fujita, A. Yamamoto, H. Yoshida, H. Tanaka, M. G. Brik, S. Tanabe, *Adv. Opt. Mater.* **2021**, *9*, 2100033.
[9] C. Mi, J. Zhou, F. Wang, G. Lin, D. Jin, *Chem. Mater.* **2019**, *31*, 9480.
[10] P. Wang, M. Ding, L. Bo, C. Guan, Y. Semenova, Q. Wu, G. Farrell, G. Brambilla, *Opt. Lett.* **2013**, *38*, 4617.
[11] E. Martín Rodríguez, G. López-Peña, E. Montes, G. Lifante, J. García Solé, D. Jaque, L. A. Diaz-Torres, P. Salas, *Appl. Phys. Lett.* **2017**, *111*, 081901.
[12] L. Marciniak, A. Bednarkiewicz, D. Kowalska, W. Strek, *J. Mater. Chem. C* **2016**, *4*, 5559.
[13] M. Back, J. Ueda, J. Xu, K. Asami, M. G. Brik, S. Tanabe, *Adv. Opt. Mater.* **2020**, *8*, 2000124.
[14] L. Marciniak, A. Bednarkiewicz, J. Drabik, K. Trejgis, W. Strek, *Phys. Chem. Chem. Phys.* **2017**, *19*, 7343.
[15] K. Elzbieciak-Piecka, J. Drabik, D. Jaque, L. Marciniak, *Phys. Chem. Chem. Phys.* **2020**, *22*, 25949.
[16] X. Zhao, J. Yan, H. Bao, Y. Dan, *AIP Adv.* **2019**, *9*, 015107.
[17] H. Lin, S. Mao, H. Zeng, Y. Zhang, M. Kawaguchi, Y. Tanaka, J.-M. Lin, K. Uchiyama, *Anal. Chem.* **2019**, *91*, 7346.
[18] K. Shimanovich, Z. Mutsafi, Y. Roizin, Y. Rosenwaks, *J. Phys. D: Appl. Phys.* **2019**, *53*, 065101.
[19] J. Feng, M. Ding, J. Kou, F. Xu, Y. Lu, *IEEE Photon. J.* **2011**, *3*, 810.
[20] J. long Kou, J. Feng, L. Ye, F. Xu, Y. qing Lu, *Opt. Express* **2010**, *18*, 14245.
[21] G. Liu, Q. Sheng, W. Hou, M. Han, *Opt. Lett.* **2016**, *41*, 5134.
[22] A. Luchechko, V. Vasyltsiv, Y. Zhydachevskyy, M. Kushlyk, S. Ubizskii, A. Suchocki, *J. Phys. D: Appl. Phys.* **2020**, *53*, 354001.
[23] V. Mykhaylyk, H. Kraus, Y. Zhydachevskyy, V. Tsiumra, A. Luchechko, A. Wagner, A. Suchocki, *Sensors* **2020**, *20*, 18.
[24] X.-S. Wang, J.-Q. Situ, X.-Y. Ying, H. Chen, H. fei Pan, Y. Jin, Y.-Z. Du, *Acta Biomater.* **2015**, *22*, 164.
[25] X.-S. Wang, W.-S. Li, J.-Q. Situ, X.-Y. Ying, H. Chen, Y. Jin, Y.-Z. Du, *RSC Adv.* **2015**, *5*, 12886.
[26] S. J. Pearton, J. Yang, P. H. Cary, F. Ren, J. Kim, M. J. Tadjer, M. A. Mastro, *Appl. Phys. Rev.* **2018**, *5*, 011301.
[27] R. Zou, Z. Zhang, Q. Liu, J. Hu, L. Sang, M. Liao, W. Zhang, *Small* **2014**, *10*, 1848.
[28] H. Deng, K. J. Leedle, Y. Miao, D. S. Black, K. E. Urbanek, J. McNeur, M. Kozák, A. Ceballos, P. Hommelhoff, O. Solgaard, R. L. Byer, J. S. Harris, *Adv. Opt. Mater.* **2020**, *8*, 1901522.
[29] M. Higashiwaki, G. H. Jessen, *Appl. Phys. Lett.* **2018**, *112*, 060401.
[30] M. Alonso-Orts, E. Nogales, B. Méndez, in *Wide Bandgap Semiconductor-Based Electronics*, 2053-2563, IOP Publishing, Bristol, UK **2020**, pp. 8-1–8-26.
[31] T. Miyata, T. Nakatani, T. Minami, *J. Lumin.* **2000**, *87-89*, 1183.
[32] E. Nogales, J. Á. García, B. Méndez, J. Piqueras, *Appl. Phys. Lett.* **2007**, *91*, 133108.
[33] E. Nogales, B. Méndez, J. Piqueras, J. A. García, *Nanotechnology* **2009**, *20*, 115201.
[34] E. Nogales, J. A. García, B. Méndez, J. Piqueras, *J. Appl. Phys.* **2007**, *101*, 033517.
[35] Y. Tokida, S. Adachi, *J. Appl. Phys.* **2012**, *112*, 063522.
[36] M. Alonso-Orts, E. Nogales, J. M. San Juan, M. L. Nó, J. Piqueras, B. Méndez, *Phys. Rev. Appl.* **2018**, *9*, 064004.
[37] M. Alonso-Orts, E. Nogales, J. M. San Juan, M. L. Nó, B. Méndez, in *Oxide-based Materials and Devices X* (Eds: D. J. Rogers, D. C. Look, F. H. Teherani), Vol. *10919*, SPIE, Bellingham, WA **2019**, pp. 103–109.
[38] D. Dohy, G. Lucazeau, A. Revcolevschi, *J. Solid State Chem.* **1982**, *45*, 180.
[39] C. Kranert, C. Sturm, R. Schmidt-Grund, M. Grundmann, *Sci. Rep.* **2016**, *6*, 35964.
[40] C. Bradac, S. F. Lim, H.-C. Chang, I. Aharonovich, *Adv. Opt. Mater.* **2020**, *8*, 2000183.

[41] E. Nogales, B. Méndez, J. Piqueras, *Appl. Phys. Lett.* **2005**, *86*, 113112.
[42] Z. Chen, S. Xiong, S. Gao, H. Zhang, L. Wan, X. Huang, B. Huang, Y. Feng, W. Liu, Z. Li, *Sensors* **2018**, *18*, 1.
[43] W. Mu, Z. Jia, Y. Yin, Q. Hu, Y. Li, B. Wu, J. Zhang, X. Tao, *J. Alloys Compd.* **2017**, *714*, 453.
[44] F. Orlandi, F. Mezzadri, G. Calestani, F. Boschi, R. Fornari, *Appl. Phys. Express* **2015**, *8*, 111101.
[45] I. Bhaumik, R. Bhatt, S. Ganesamoorthy, A. Saxena, A. K. Karnal, P. K. Gupta, A. K. Sinha, S. K. Deb, *Appl. Opt.* **2011**, *50*, 6006.
[46] N. W. Gong, M. Y. Lu, C. Y. Wang, Y. Chen, L. J. Chen, *Appl. Phys. Lett.* **2008**, *92*, 073101.
[47] I. López, E. Nogales, B. Méndez, J. Piqueras, *Appl. Phys. Lett.* **2012**, *100*, 261910.